Snapshot imaging spectropolarimeter utilizing polarization gratings

Jihwan Kim and Michael J. Escuti

North Carolina State Univ, Dept Electrical & Computer Engineering, Raleigh, NC (USA)

ABSTRACT

Measurements of complete polarization and spectral content across a broad wavelength range of a scene are used in various fields including astronomy, remote sensing, and target detection. Most current methods to acquire spectral and polarimetric information need moving parts or modulation processes which lead to significant complexity or reduce sampling resolution. Here we present a novel snapshot imaging spectropolarimeter based on anisotropic diffraction gratings known as polarization gratings (PGs). Using multiple PGs and waveplates, we can acquire both spectrally dispersed and highly polarized diffractions of a scene on a single focal plane array, simultaneously. PGs uniquely produce only three diffracted orders (0 and ±1), polarization independent zeroth-order, polarization sensitive first-orders that depend linearly with the Stokes parameters, and easily fabricated as polymer films suitable for visible to infrared wavelength operation. The most significant advantage of our spectropolarimeter over other snapshot imaging systems is its capability to provide simultaneous acquisition of both spectral and polarization information at a higher resolution and in a simpler and more compact way. Here we report our preliminary data and discuss the cogent design of our imaging spectropolarimeter.

Keywords: Spectrometry, polarimetry, spectropolarimeter, imaging spectrometry, polarization grating, liquid crystals, reactive mesogens, remote sensing

1. INTRODUCTION

Measurement of spectral and polarization information from a scene has become of interest in various fields including astronomy, remote sensing, and biomedical imaging/diagnosis. Since most detectors (i.e., CCDs) can measure only intensity, detection of spectral and/or polarization can be done by special techniques; for instance, tunable filters or diffraction gratings for wavelength separation and rotating waveplates betweeen crossed polarizers for polarization detection. Our approach to imaging spectropolarimetry involves transmissive anisotropic diffraction gratings known as polarization gratings (PGs).[1–3] With this novel diffractive element, we can acquire spectrally dispersed and highly polarization-sensitive diffractions of a scene on a single focal plane array. We apply iterative algorithms to reconstruct four-dimensional information of the image which contains two spatial variables (x, y), spectral variable (λ), and the Stokes parameters $(S_i,\ i = 0, 1, 2, 3)$.

Correspondence should be sent to: mjescuti@ncsu.edu, Telephone: +1 919 513 7363

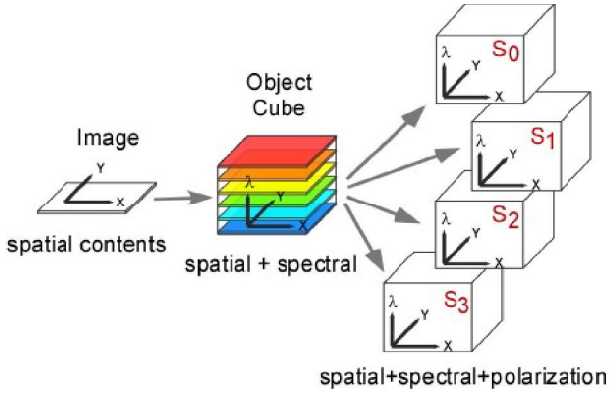

Figure 1. The representation of data cubes (4D) containing spectral and polarimetric information from a 2D scene.

Imaging Spectrometry XIII, edited by Sylvia S. Shen, Paul E. Lewis, Proc. of SPIE Vol. 7086, 708603, (2008) · 0277-786X/08/$18 · doi: 10.1117/12.795719

2. BACKGROUND

2.1 Snapshot Imaging Spectropolarimetry Techniques

Nonscanning imaging system to estimate high-dimensional object from the two-dimensional projection was suggested with computed-tomography concepts. To measure both the spatial and the spectral content of an object scene, the computed tomography imaging spectrometer (CTIS)[4–6] employed transmission phase gratings or computer generated hologram disperser to make dispersion patterns without any scanning. Recently, Dereniak et al. introduced and developed a technique to achieve snapshot spectropolarimetry[7–10] using thick birefringent plates and polarizer. Despite its novelty and snapshot capability, spectral modulation and post-processing in the CTICS limit the spectral resolution and detection speed, respectively. However, design we introduce here avoids these limitations by using unique polarization diffraction properties of PGs. Since PGs spatially separate different polarizations as well as wavelengths, simultaneous measurement of spectral and polarization can be done by a single element. A proper combination of PGs and $\lambda/4$-waveplates aligned at different angles makes it possible to project complete spectral and polarization information with the two dimensional dispersion patterns, which can be focused on a single focal plane array. Then, image reconstruction from the dispersion patterns can be done by computed tomography techniques. Our approach is uniquely compelling as it provides capability of snapshot spectropolarimetry on the single detector without moving/tuning parts or spectral modulation. In addition, robust, compact and lightweight thin-film assembly of the design can be adopted with conventional imaging systems.

2.2 Polarization Grating Properties

The essence of our approach is a reactive mesogen (polymerizable liquid crystal)[11,12] film with a continuous periodic alignment pattern that can be classified as a Polarization Grating[2,13,14] (PG). Unlike amplitude and phase gratings, PGs operate by locally modulating the polarization state of light passing through, and the wavelength separation occurs by the grating equation since the PGs are merely birefringent gratings. PGs have been studied for many applications, including microdisplays,[15] tunable filters,[16] spectrophotometers,[17] and beam steerers.[18] Recently, we demonstrated an achromatic PG[1] that accomplishes both chromatic and polarization separation with ~100% efficiency across the entire visible wavelength range. As shown in Fig. 2(b), this achromatic PG comprises of two antisymmetric chiral PGs with opposite twist sense, where the nematic director **n** follows:

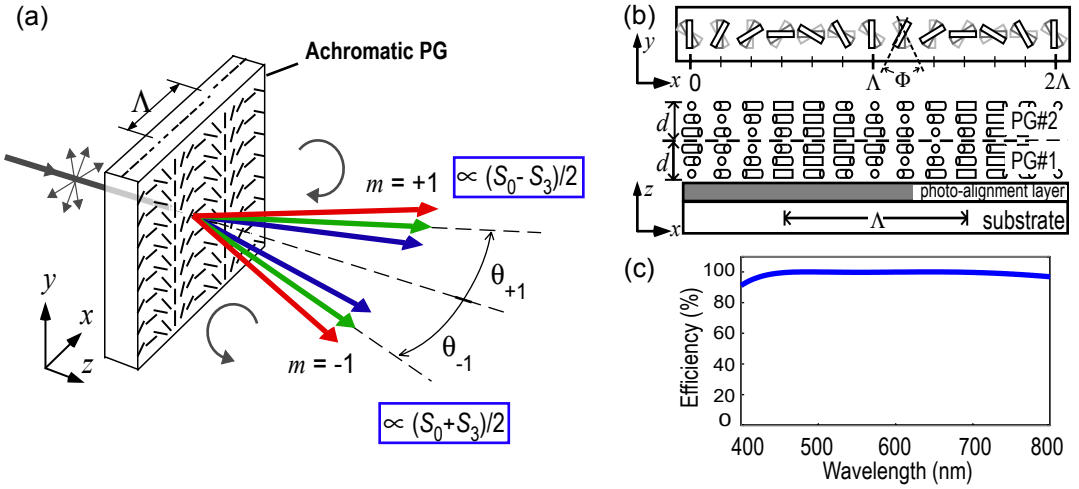

Figure 2. (a) Diffraction geometry and behavior of the Achromatic Polarization Grating (PG) (note only the $m = 0, \pm 1$ orders are transmitted, according to Eqs. 2); (b) Nematic director profile of Achromatic PG and side-view (following Eqs. 1); (c) Total first-order diffraction efficiency ($\Sigma\eta_{\pm 1}$).

$$\mathbf{n}(x,z) = [\cos\phi(x,z),\ \sin\phi(x,z),\ 0] \tag{1a}$$

$$\phi(x,z) = \begin{cases} \pi x/\Lambda + \Phi z/d & \text{if } 0 \le z \le d \\ \pi x/\Lambda - \Phi z/d + 2\Phi & \text{if } d < z \le 2d \end{cases} \tag{1b}$$

where ϕ is the azimuth angle of the director field, Λ is the grating period, d is the thickness, and Φ is the twist angle of each chiral layer.

The diffraction efficiency η_m of order m may be calculated using Jones calculus.[1,19]

$$\eta_0 = \left[\cos^2 X + \left(\Phi^2 - \Gamma^2\right)\,\mathrm{sinc}^2 X\right]^2 \tag{2a}$$

$$\eta_{\pm 1} = A^2 \left(\frac{1 \mp S_3'}{2}\right)\left(\cos^2 X + \Phi^2\,\mathrm{sinc}^2 X\right) \tag{2b}$$

where $\Gamma = \pi\Delta nd/\lambda$, $X = \sqrt{\Phi^2+\Gamma^2}$, $A = 2\Gamma\,\mathrm{sinc}\,X$, and $\mathrm{sinc}\,X \equiv (\sin X)/X$. The term $S_3' = S_3/S_0$ is a normalized Stokes parameter of incident light (Fig. 2(a)). Fig. 2(c) shows the first order diffraction efficiency spectrum for $\Phi = 70°$. We will assume a polarization grating as an achromatic PG in this paper without notice.

Several important properties should be noted in Eqs. (2). First, only three diffraction orders (0 and ± 1) exist, which depend on both the retardation $\Delta nd/\lambda$ and the twist angle Φ. We will show that $\Sigma\eta_{\pm 1} \approx 100\%$ over a wide wavelength range by balancing the effect of retardation and twist. Second, the first orders have orthogonal circular polarizations (Fig. 2(b)). Third, the first-order efficiencies are strongly sensitive to the incident polarization state through S_3'. With proper combinations of a PG and a quater waveplate (QWP), other polarization states (S_1 and S_2) can be analyzed. When multiple PGs and QWPs are combined, it is possible to separate the complete polarization information corresponding all four Stokes parameters ($S_{0,1,2,3}$) in diffracted patterns at the same time. We now consider a combination of a PG and a QWP having its symmetry axis at X-axis ($\theta = 0°$), and the diffraction efficiency of the first orders can be written as;

$$\eta_{\pm 1} = A^2 \left(\frac{1 \pm S_2'}{2}\right)\left(\cos^2 X + \Phi^2\,\mathrm{sinc}^2 X\right) \tag{3}$$

where $S_2' = S_2/S_0$ is the normalized Stokes parameter corresponding to component of incident light linearly polarized in the $\pm 45°$ directions. With two QWPs ($\theta = 0°, 45°$) placed before a PG, the first-order efficiency can be written as:

$$\eta_{\pm 1} = A^2 \left(\frac{1 \mp S_1'}{2}\right)\left(\cos^2 X + \Phi^2\,\mathrm{sinc}^2 X\right) \tag{4}$$

where $S_1' = S_1/S_0$ is the normalized Stokes parameter corresponding to component of incident light linearly polarized in the horizontal and vertical directions. The zeroth-order remains same as Eq. 2a since it is independent to polarization. Note that the paraxial approximation and a thin grating with the infinite width at normal indicence are assumed to derive the analytical expressions for diffraction efficiencies.

2.3 Reconstruction Algorithm

Imaging spectropolarimeters extract high dimensional information (spatial, spectral and polarization) from a scene using a low dimensional detector array (1D or 2D). To find high dimensional information from the low dimensional known, most conventional systems generally employ moving parts or multiple detections which lead to undesirable reliability issues. Especially, to extract the information from the moving target, simultaneous detection of a scene is essential to prevent the artifacts of the results. In order to avoid the problem, Okamoto suggested a technique[20] based on the computed tomography (CT)[21–23] that allows simultaneous acquisition of spectral image information with transmission gratings and monochromatic camera. Since CT is an indirect imaging system where projected images from a object scene are overlapped on the same detector, special techniques are required to reconstruct information in higher dimensions (i.e., 2D spatial images across many wavelengths). As shown in Fig. 3, multi-dimensional object $\mathbf{f}$ can be projected as a dispersed images $\mathbf{g}$ on a two-dimensional

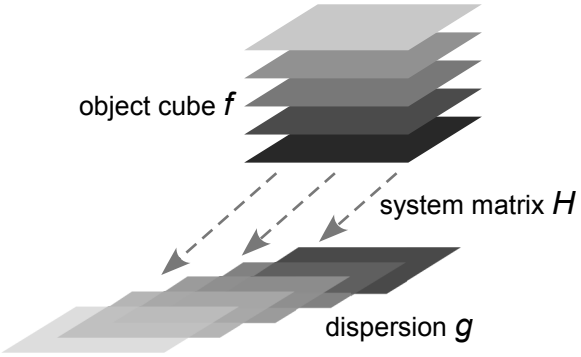

Figure 3. The diffraction of PG causes the spectral dispersion on the detector array. Object can be representative as data cube which contain spectral and polarimetric information of the scene.

space by a system with its system matrix $\mathbf{H}$. Generically, the system is described by $\mathbf{g} = \mathbf{Hf}$.[24] Once the projected dispersion $\mathbf{g}$ is obtained from a detector, the actual object cube $\mathbf{f}$ can be estimated by iterative algorithms such as the multiplicative algebraic reconstruction techniques (MART):[25,26]

$$\mathbf{MART}: \hat{f}_n^{(k+1)} = \hat{f}_n^{(k)} \frac{\left(\mathbf{H}^T g\right)_n}{\left(\mathbf{H}^T \mathbf{H} \hat{\mathbf{f}}^{(k)}\right)_n} \tag{5}$$

where $\hat{\mathbf{f}}$ is an estimate of the object data. The iterative algorithms require more computational time to acquire relatively higher resolution, however, they are still attractive methods for adopting the snapshot imaging systems.

3. DESIGN OF POLARIZATION GRATING BASED IMAGING SPECTROPOLARIMETER (PGIS)

3.1 System Layout

In this paper, we introduce a new imaging spectropolarimeter design named as the Polarization Grating based Imaging Spectropolarimeter (PGIS) that utilizes liquid crystal diffraction gratings, also known as polarization gratings (PGs). PGs have only three diffraction orders and diffraction angles are governed by the grating period. Moreover, PG functions as polarization separator since the first orders from the PG are highly sensitive to polarization state of light (Sec. 2.2). With these unique properties of PG, we design the spectropolarimeter which can make diffractions selectively sensitive to each polarization state.

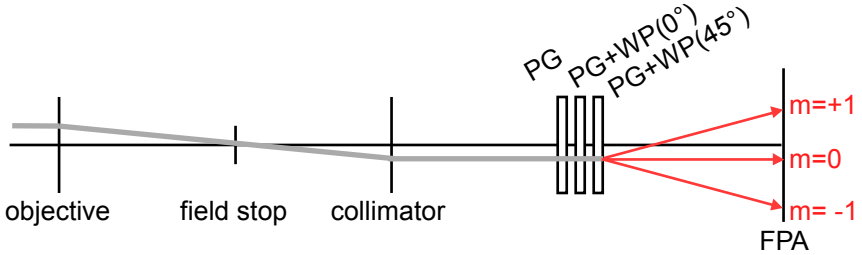

Figure 4. PGIS conceptual layout.

The layout involves dispersed imaging through PGs with the result that the imaged scene is dispersed into a rectangular array or prismatic images. By placing a field stop at a conjugate plane to the FPA, we can limit the spatial extent of the sene imaged, allowing the prismatic images to be spatially separated. This layout is the concept of our spectropolarimeter, and it is not optimized for realistic physical system setup. The layout of the PGIS includes a minimum number of elements that are necessary for extracting the complete spectral and polarization information of a scene. Additional PGs and waveplates may be included to make different dispersion patterns as interlacing them each other.

3.2 Transfer function

In optical image formation, the *object*, which is denoted by f comprises N-dimensional information distribution. In the PGIS design, *object* has four-dimensional information including two spatial coordinates, wavelength, and polarization. We can define the function $f(\mathbf{r}, \lambda, S_i)$ with $\mathbf{r}$ (spatial vector) and S_i (Stokes parameters, $i = 0, 1, 2, 3$). If the *object* is the *noise-free space* and it can be mapped to two-dimensional *image* space, $g(\mathbf{r}')$, with a linear process, then mathematically g is a linear superposition of the values of f and therefore it is given by

$$g(\mathbf{r}') = \sum_{i=0}^{3} \int\int\int f(\mathbf{r}, \lambda, S_i)\, h(\mathbf{r}, \lambda, S_i : \mathbf{r}')\, d\mathbf{r} d\lambda. \tag{6}$$

where the $h(\mathbf{r}, \lambda, S_i : \mathbf{r}')$ is a function which contains polarization and geometric mapping information between *object* and *image* spaces. When the *object* is given by $f(\mathbf{r},\lambda,S_i)$, the function of h tells the probabillity that a light coming from the *object* will be projected at the image space $g(\mathbf{r}')$, and it has a different polarization response depending on the combination of polarization gratings and waveplates. The Fig. 5 illustrates the simple

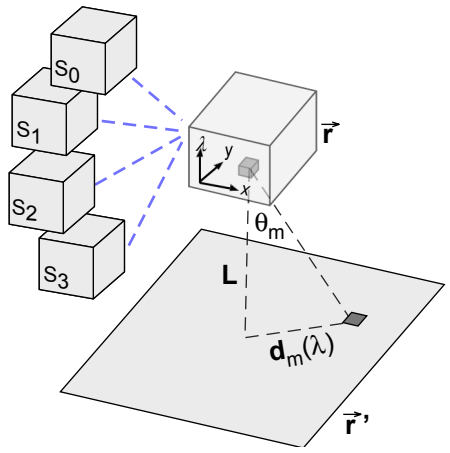

Figure 5. Geometric mapping between *object* and *image* spaces.

geometric relationship between the projections and diffracted patterns. Representing the *object* with a cube, four different cubes may be considered for all Stokes parameters (S_i, $i = 0, 1, 2, 3$). Again, the diffraction angles are determined by the grating equation as follows

$$\sin\theta_m = \left(m\frac{\lambda}{\Lambda}\right) + \sin\theta_{in}, \tag{7}$$

where θ_{in} is the incident angle, θ_m is the angle of diffraction of transmitted light, and $m = \{0, \pm 1\}$ is the diffraction order. Assuming a collimated light coming to PGs, the displacement by diffraction on the focal plane array (FPA) can be derived with a diffraction angle $\theta_m(\lambda)$.

$$d_m(\lambda) = L \cdot \tan\theta_m(\lambda), \tag{8}$$

where the L is a distance between the PG assembly and the FPA, and $\theta_m(\lambda)$=$\sin^{-1}(\mathrm{m}\lambda/\Lambda)$.

Then, the diffraction displacement vector on the imaging space can now be described with a unit vector $\hat{\mathbf{r}}'$, which defines the azimuth angle of diffractions.

$$\mathbf{d}_m(\lambda) = d_m(\lambda) \cdot \hat{\mathbf{r}}', \tag{9}$$

In the aspect of photodector, measured power is a integration of the 4D object along a particular path, which is determined by the property of diffractive element. In our case, the path will be in S0∼S3 cube depending on the PG combination as discussed in Sec.3.1. The path will be a vertical line for zero-order transmition and

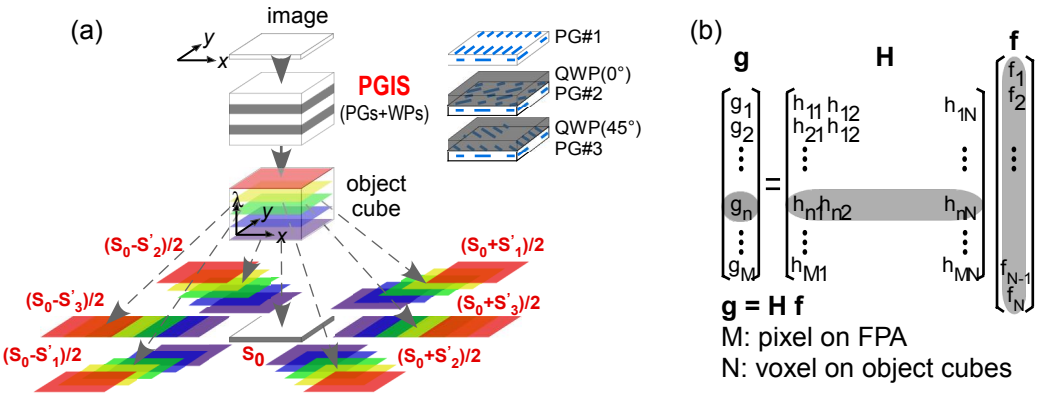

Figure 6. (a) Conceptual design of PGIS and dispersion patterns; (b) Discrete representation of the system with a linear imaging equation

nearly diagonal line for the first-order. With the consideration of spatial($\mathbf{r}$) and spectral(λ) dimensions, The paths through the object can be represented as Dirac-δ functions:[27]

$$\delta\{\mathbf{r}' - (\mathbf{r} + \mathbf{d}_m(\lambda))\} \tag{10}$$

According to the PG and QWP combination, the polarization sensitivity of the first orders are different. There can be three type of combinations ($PG_{\#N}$, $N = 1, 2, 3$), and their polarization sensitivities of each diffraction order are below:

1. $PG_{\#1}$ (PG+WP(0°)+WP(45°)): $I_{\pm1} = \propto$(S0 $\mp$ S1)/2, $I_0 = \propto$ S0.
2. $PG_{\#2}$ (PG+WP(0°)): $I_{\pm1} = \propto$(S0 $\pm$ S2)/2, $I_0 = \propto$ S0.
3. $PG_{\#3}$ (only PG): $I_{\pm1} = \propto$(S0 $\mp$ S3)/2, $I_0 = \propto$ S0.

where I_m is the output powers of the m^{th}-orders ($m = 0, \pm1$).

Using the additional Dirac-δ function for the Stokes parameters, the transfer function can be derived as:

$$h\left(\mathbf{r}, \lambda, S_i : \mathbf{r}'\right) = \delta\{\mathbf{r}' - (\mathbf{r} + \mathbf{d}_m(\lambda))\}\{A\delta(S_0 - S_i) - B\delta(S_j - S_i)\}, \tag{11a}$$

$$A = (1 + \lambda(m))/2, \tag{11b}$$

$$B = m/2 \ (m = 0, \pm1), \tag{11c}$$

when j corresponds to the type of PG combination (i.e. j=1 when $\mathrm{PG}_{\#1}$). For a simple calculation we assume the all diffractions have the unity diffraction efficients.

Then the system function can now be described as

$$g(\mathbf{r}') = \sum_{i=0}^{3} \int\int\int f\left(\mathbf{r}, \lambda, S_i\right) \delta\left\{\mathbf{r}' - (\mathbf{r} + \mathbf{d}_m(\lambda))\right\}\left\{A\delta(S_0 - S_i) - B\delta(S_j - S_i)\right\} d\mathbf{r}d\lambda, \tag{12}$$

where j follows the PG combination number. This continuous function provides the analytic relationship between 4D and 2D spaces accurately. By using this mapping information, we can finally express system matrix $\mathbf{H}$ after determining the spatial and spectral resolutions of object.

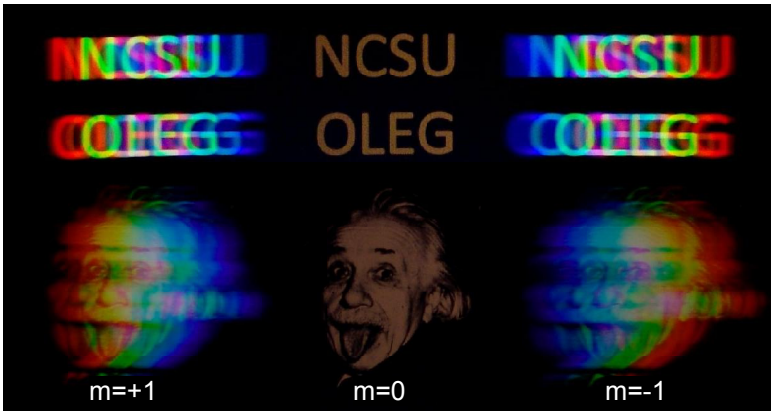

Figure 7. Dispersion pattern of images as seen through a PG.

3.3 Imaging Reconstruction

Fig. 6(a) shows the proposed PGIS design using combination of PGs and QWPs interlaced with each other. Due to the angular dispersion from the polarization sensitive diffraction of PGs, both spectral and polarization information from the input image is projected onto the FPA. According to the combination of PG and QWP, each of the diffracted patterns in Fig. 6(a) exhibits different polarization sensitivity, as indicated by the respective Stokes parameters, and is also a superposition of the wavelength content in the scene. In the previous section, we described this system in a continuous manner, however, *object* and *image* spaces should be considered discrete since all data from the detector is discrete. Detected data from the discrete sensor arrays, **g**, can be related to the discrete volume units in the *object* space and all this volumetic information can be represented by object vector **f**. The relationship betweem these discrete vectors, **f** and **g**, can be described by the system matrix **H** which has all the positional and polarization information of these projections (Fig. 6(b)). Using the reconstruction algorithm (Sec. 2.3), estimation of object **f** can be obtained from a measured image **g** with an inversion of system matrix **H**.

4. SIMULATION RESULTS

4.1 Diffracted image from single PG

Fig. 7 illustrates the chromatic dispersion of color images from a PG captured by a digital camera. The image shown is displayed as a wallpaper over a dark background on an LCD monitor, and an achromatic PG with 6μm grating pitch was placed in front of it. The camera was positioned behind the PG and focused on the diffracted orders, with the distance between the PG and the image adjusted to provide sufficient angular dispersion. Achromatic PG of 6μm graing period was located in front of the camera following the x-axis of image but we could make different angular dispersion as simply changing the optical axis of PG. Light coming from the monitor is linearly polarized (no circular polarization (S_3) component). Hence from Eq. 2b, the intensities of the first diffracted orders should be the same. We can observe almost same intensities of the first orders in Fig. 7 and there are only three chromatic dispersions since the light has three color sources (R,G,B).

4.2 Spectral image reconstruction

For the simple test image having only spectral variation, we created a virtual *object*. The images for each wavelength is spatially uniform but spectrally different. The grayscale of these images increses from 0(black) to 1(white) as their wavelengh increases, with resolution fixed at 32×32 pixels. A detector is a noiseless pixel array and three PGs are used to create the dispersion patterns. Fig. 8(a) shows one of the dispersion patterns generated by simulation and 7 spectral images are overlapped with nonlinear offsets between them. Fig. 8(b) compares the original object with the reconstructed object. We can calculate the normalized root mean square

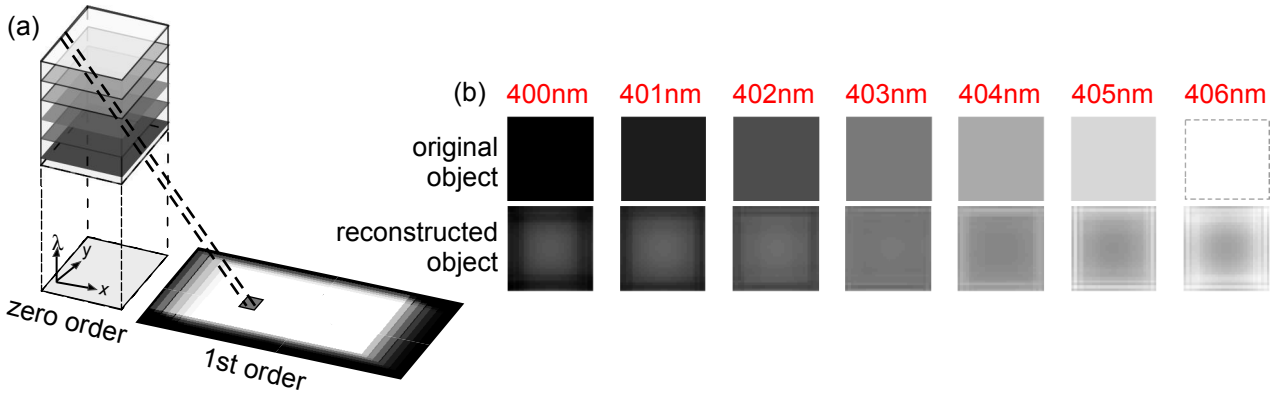

Figure 8. Spectrometry simulation: 32×32×7 spatially uniform test images are reconstructed with 3 PG-combinations

error (RMSE) as:

$$\mathrm{RMSE} = \left(\sum_{m=1}^{M} \frac{1}{M} (f_m - \hat{f}_m)^2 \right)^{1/2}, \tag{13}$$

where M is the number of unit object (number of entry in vector $\mathbf{f}$) and f_{mean} is the mean value for unit objet. Calculated RMSE is 0.129 and overall it appears that the system works reasonably for this simple spectral test image.

4.3 Spectral and polarimetric image reconstruction

In a second simulation, we test with virtual *object* which has both spectral and polarization variation. To show the small difference between the spectral images, we used the motion images of a tiger. Moreover, we assume different regional polarization sensitivity and manipulate each spectral image to add the polarization information of them. For example, the light from the nose of the tiger is partially related to linearly polarized light (S_1) in the horizontal and vertical directions. In the same manner, the light corresponding to the tongue of the tiger and the background are linearly polarized in the diagonal direction, (S_2) and circularly polarized (S_3) respectively (Fig. 9(a)). We simulated this with 6 PG-combinations ($2\times PG_{\#N}$, $N = 1, 2, 3$), so totally 6 PGs and 4 QWPs are used. Dispersion patterns are shown in Fig. 9(b) and each pattern is related to each PG-combination. The image resolution is 32×32 pixels and 9 images are using for different wavelengths with spectral resolution of 1nm. Fig. 10 shows the simulation result of Spectral and polarimetric image reconstruction. The top figures are original *object* and lower figures are reconstructed *object*. For the imaging reconstruction, MART is used with 10 iterations. There are several peak errors, but all reconstructed images generally follow the same values of the original images and moreover, most of polarized regions are recognizable. We can observe

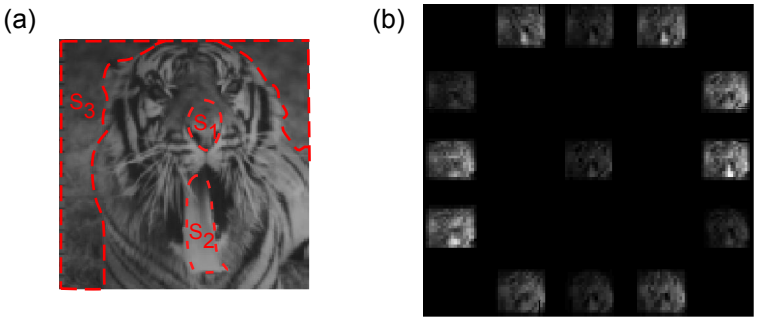

Figure 9. (a) One of the test image (high-resolution); simulated images are down-sampled as 32×32 and manipulated to add polarization information. (b) Simulated dispersion spectrum; We can check the panchromatic image at the zero-order projection of dispersion spectrum

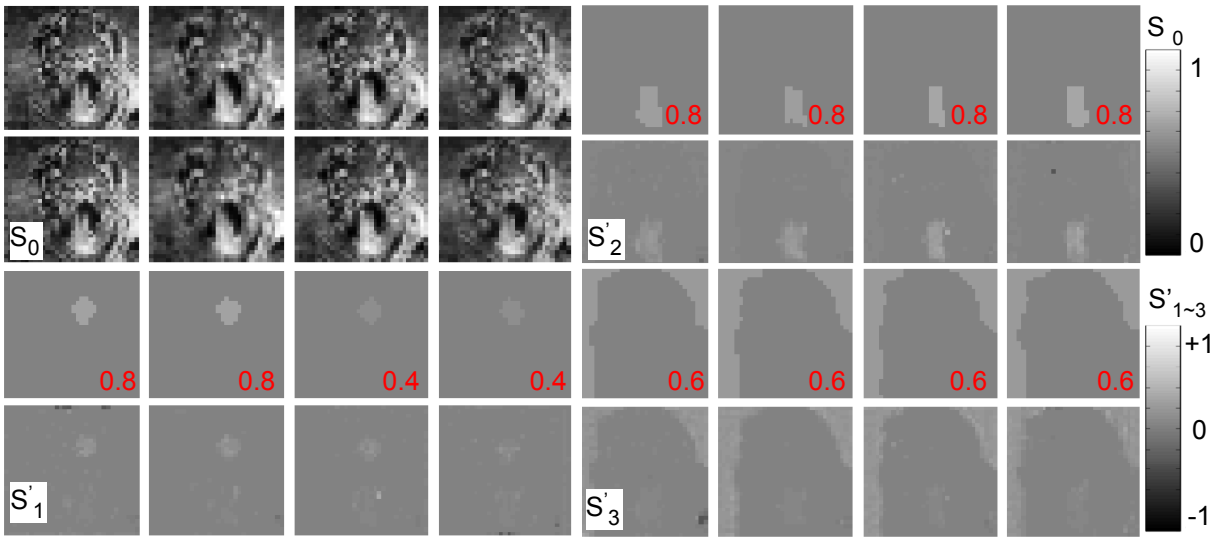

Figure 10. Spectropolarimetry simulation; 32×32×9 test images are reconstructed with 6 PG-combinations (shown only 4 images).

that S_0 reconstructions are better than others since S_0 information is detected for all of dispersion patterns (for the zero-order transmittance, there is only zero order). For this simulation, the size and number of samples are relatively small and spectral variation of images are not large and so the results are acceptable, but we need to calculate the error rate with another test sample.

5. CONCLUSIONS

We have introduced the concept of Polarization Grating based Snapshot Imaging Spectropolarimetry (PGIS). We employ multiple PGs to create chromatic dispersion patterns that are linearly proportional to Stokes vector (polarization information) embedded in a scene. We show an imaging system which produces a 2D projection on the FPA from a 4D object containing spatial, spectral and polarization informaiton. Using simulated images and the PGIS concept PGIS, spectral and polarimetric information of a scene was successively reconstructed. PGIS may have capability to reconstruct the object with higher resolution in all dimensions since it can estimate 4D object from the dispersion patterns without Fourier-domain post-processing, and may allow a faster overall reconstruction than current snapshot imaging spectropolarimeter approaches. We aim to continue this development toward a more optimal and practical device implementation and theoretical analysis.

ACKNOWLEDGMENTS

The authors gratefully acknowledge support from the National Science Foundation (grant ECCS-0621906), and productive discussions with Chulwoo Oh.

REFERENCES

1. C. Oh and M. J. Escuti, "Achromatic diffraction from polarization gratings with high efficiency," *Optics Letters* **7093**, Accepted, 2008.
2. C. Oh and M. J. Escuti, "Numerical analysis of polarization gratings using the finite-difference time-domain method," *Physical Review A* **76**(4), p. 043815, 2007.
3. G. P. Crawford, J. N. Eakin, M. D. Radcliffe, A. Callan-Jones, and R. A. Pelcovits, "Liquid-crystal diffraction gratings using polarization holography alignment techniques," *Journal of Applied Physics* **98**(12), p. 123102, 2005.
4. M. Descour and E. Dereniak, "Computed-tomography imaging spectrometer - experimental calibration and reconstruction results," *Applied Optics* **34**(22), pp. 4817–4826, 1995.

5. C. E. Volin, J. P. Garcia, E. L. Dereniak, M. R. Descour, T. Hamilton, and R. McMillan, "Midwave-infrared snapshot imaging spectrometer," *Optical Engineering* **40**(25), pp. 4501–4506, 2001.
6. W. R. Johnson, D. O'Connell, E. L. Dereniak, and E. K. Hege, "Novel calibration recovery technique for an expectation maximization tomographic reconstruction," *Optical Engineering* **43**(1), pp. 10–11, 2004.
7. D. Sabatke, A. Locke, E. L. Dereniak, M. Descour, J. Garcia, T. Hamilton, and R. W. McMillan, "Snapshot imaging spectropolarimeter," *Optical Engineering* **41**(5), pp. 1048–1054, 2002.
8. N. Hagen, E. L. Dereniak, and D. T. Sass, "Visible snapshot imaging spectro-polarimeter," *Proc. SPIE* **5888**, p. 588810, 2005.
9. W. R. Johnson, D. W. Wilson, and G. Bearman, "Visible snapshot imaging spectro-polarimeter," *Appl. Opt.* **45**(9), pp. 1898–1908, 2006.
10. R. Aumiller, C. Vandervlugt, E. Dereniak, R. Sampson, and R. McMillan, "Snapshot imaging spectropolarimetry in the visible and infrared," *Proc. SPIE* **6972**, p. 69720D, 2008.
11. D. J. Broer, "Insitu photopolymerization of oriented liquid-crystalline acrylates 3 oriented polymer networks from a mesogenic diacrylate," *Macromol. Chem. Phys.* **190**, pp. 2255–2268, 1989.
12. S. M. Kelly, "Anisotropic networks," *J. Mater. Chem.* **5**, pp. 2047–2061, 1995.
13. L. Nikolova and T. Todorov, "Diffraction efficiency and selectivity of polarization holographic recording," *Optica Acta* **31**(5), pp. 579–588, 1984.
14. J. Tervo and J. Turunen, "Paraxial-domain diffractive elements with 100% efficiency based on polarization gratings," *Optics Letters* **25**(11), pp. 785–786, 2000.
15. R. K. Komanduri, W. M. Jones, C. Oh, and M. J. Escuti, "Polarization-independent modulation for projection displays using small-period LC polarization gratings," *Journal of the Society for Information Display* **15**(8), pp. 589–594, 2007.
16. E. Nicolescu and M. J. Escuti, "Polarization-independent tunable optical filters based on liquid crystal polarization gratings," *Proc. SPIE* **6654**(1), 2007.
17. E. Nicolescu and M. J. Escuti, "Compact spectrophotometer using polarization-independent liquid crystal tunable optical filters," *Proc. SPIE* **6661**(1), 2007.
18. J. Kim, C. Oh, M. J. Escuti, L. Hosting, and S. Serati, "Wide-angle nonmechanical beam-steering using thin liquid crystal polarization gratings," *Proc. SPIE* **7093**, 2008.
19. C. Oh and M. J. Escuti, "Achromatic polarization gratings as highly efficient thin-film polarizing beamsplitters for broadband light," *Proc. SPIE* **6682**, p. 668211, 2007.
20. T. Okamoto and I. Yamaguchi, "Simultaneous acquisition of spectral image information," *Opt. Lett.* **16**, pp. 1277–1279, 1991.
21. R. Gordon, "A tutorial on art (algebraic reconstruction technique)," *IEEE Trans. on Nuclear Science* **21**, pp. 78–93, 1974.
22. A. C. Kak and M. Slaney, *Principles of computerized tomographic imaging*, IEEE Press, 1998.
23. M. Bertero and P. Boccaci, *Introduction to inverse problems in imaging*, Institute of Physics Pub., 1998.
24. H. H. Barrett and K. Meyers, *Foundations of Image Science*, Wiley, 2003.
25. C. L. Byrne and J. Graham-Eagle, "Image iterative reconstruction algorithms," *Proc. SPIE* **1767**, pp. 83–92, 1992.
26. A. Lent, "A convergent algorithm for maximum entropy image restoration with a medical x-ray application," *Soc. Phot. Sci. and Eng.* , pp. 249–257, 1976.
27. M. Y. Chiu and H. H. Barrett, "Three-dimensional radiographic imagign with a restricted view angle," *J. Opt. Soc. Am.* **83**, pp. 325–330, 1979.